Temperature- and depth-dependent valence band electronic structures of half-metallic Co_2MnSi studied by hard x-ray photoemission spectroscopy

Shigenori Ueda[1,2,*], Yuichi Fujita[3,4,†], Ivan Kurniawan[3], Yuya Sakuraba[3], and Yoshio Miura[3,5,6]

[1]*Research Center for Electronic and Optical Materials, National Institute for Materials Science (NIMS), Tsukuba, Ibaraki 305-0044, Japan*

[2]*Synchrotron X-ray Station at SPring-8, NIMS, Sayo, Hyogo 679-5148, Japan*

[3]*Research Center for Magnetic and Spintronic Materials, NIMS, Tsukuba, Ibaraki 305-0047, Japan*

[4]*International Center for Young Scientists, NIMS, Tsukuba, Ibaraki 305-0047, Japan*

[5]*Graduate School of Engineering Science, Kyoto Institute of Technology, Sakyo-ku, Kyoto 606-8585, Japan*

[6]*Center for Spintronics Research Network, Graduate School of Engineering Science, The University of Osaka, Toyonaka, Osaka 560-8531, Japan*

Abstract

Temperature(T)- and depth-dependent valence band (VB) electronic structures of an AlO_x-capped $L2_1$-ordered Co_2MnSi (CMS) thin film were studied by hard x-ray photoelectron spectroscopy (HAXPES) combined with x-ray total reflection (TR) to reveal the electronic states of the inside of CMS film (bulk) and near-interface region of CMS beneath the AlO_x layer. The depth-dependent magnetic states of Co and Mn in CMS were also studied by magnetic circular dichroism (MCD) in core-level HAXPES measurements combined with TR. The VB HAXPES spectra obtained at T = 20, 100, 200, and 300 K showed the clear T dependence in the spectral shapes for both the near-interface and bulk regions of CMS, but the T dependence of electronic states between the near-interface and bulk regions are different as well as the T-dependent magnetization of CMS for the near-interface and bulk regions obtained by the Co and Mn 2p core-level MCD-HAXPES measurements. The T-dependent VB HAXPES spectra of CMS in the bulk region qualitatively agreed with the electronic structure calculations with the disordered local moment method for bulk CMS, indicating the importance of the spin fluctuations on the electronic states of bulk CMS at a finite T and the enhanced spin fluctuations in the near-interface region of CMS. These results suggest that the direct probing of the electronic and magnetic states of the insulator/ferromagnet heterojunctions in a non-destructive way is important to reveal the properties of ferromagnet for the near-interface and bulk regions at a finite T.

I. Introduction

Temperature (T) dependence of spin-resolved electronic states near the Fermi-level (E_F) of prototypical ferromagnetic materials (FMs) with Curie temperature (T_C) much higher than room temperature (RT) is expected to be very small in the T range between 0 K and $0.4T_C$, since the magnetization (M) of FMs is almost unchanged according to the Bloch $T^{3/2}$ law, which is given by $M(T)/M(0\ \mathrm{K}) = 1-\alpha T^{3/2}$ (α is coefficient for $T < \sim 0.4T_C$). A giant or tunnel magnetoresistance (GMR or TMR) junction, which consists of two FM layers with high T_C as top and bottom magnetic electrodes separated by a nonmagnetic metal or nonmagnetic insulator layer, has brought into applications such as read heads for hard disk drives [1] and magnetic random-access memories [2]. A TMR effect utilizes a spin-dependent transport near E_F between two FMs through an insulator, and a TMR junction exhibits a low (high) resistance state in the parallel (antiparallel) configuration of M between two FM electrodes. The performance of TMR junction is characterized by the ratio given by $(R_{AP}-R_P)/R_P$, where R_{AP} and R_P are the resistance for the M antiparallel and parallel (M_{AP} and M_P) configurations, respectively. Particularly, TMR junctions using predicted half-metals as a magnetic electrode with a barrier layer (*e.g.,* AlO_x, MgO) exhibit a huge TMR ratio, because the property of half-metals, in which the minority spin band has a band gap across E_F and the majority spin band is metallic, leading strong enhancement of R_{AP} in the M_{AP} condition due to the spin-dependent tunneling. In fact, by using the predicted half-metal of Co_2MnSi (CMS) and $Co_2(Mn,Fe)Si$ (CMFS), TMR ratios of 570% at 2 K [3], 2010% at 4.2 K [4], and 2610% at 4.2 K [5] have been reported for the CMS/AlO_x/CMS, the CMS/MgO/CMS, and CMFS/MgO/CMFS junctions, respectively. However, these TMR ratios drastically reduce to 67, 335 and 429% for the CMS/AlO_x/CMS, CMS/MgO/CMS and CMFS/MgO/CMFS junctions at around RT [3-5], respectively, in spite of that the T dependence of spin-resolved electronic states and $M(T)$ are expected to be small below RT owing to high T_C (~1000 K) of CMS and CMFS. Similarly, the GMR junction of $Co_2FeGa_{0.5}Ge_{0.5}$ (CFGG)/Ag/CFGG

also shows the reduction of GMR ratio with increasing T (285% at 10 K and 82% at RT)[6]. The strong reduction of the ratio with increasing T by the use of not only half-metallic electrodes but also prototypical ferromagnetic electrodes (such as Fe, CoFe) is unclarified yet [7], and is an issue to be solved to realize high-performance practical devices operating at RT and/or higher T.

To investigate the strong reduction of TMR ratio, the T- and spin-dependent electronic structures of $L2_1$-ordered CMS have been studied by the density functional theory (DFT) calculations [8-10] with the local spin density approximation (LSDA) or the generalized gradient approximation (GGA). The LSDA calculations combined with the dynamical mean-field theory (DMFT) for treating a finite T effect have reported the shift of the majority spin band toward E_F and the increase of the minority band states at E_F (or evolution of so-called nonquasiparticle (NQP) states) with increasing T [8]. The LSDA calculations with the disordered local moment (DLM) method for treating spin fluctuations at a finite T have also reported the increase of the minority spin states at E_F (not due to NQP states) with increasing T and weak T-dependent spin-resolved electronic states in the energy range between –4 and 4 eV relative to E_F [9]. The GGA-DLM calculations at T = 300 K have shown similar results for the LSDA-DLM calculations, even the effect of phonon has been included in the calculations [10]. Although M(300 K) is ~0.98 times of M(0 K) for bulk CMS due to high T_C as referred to the $M(T)$ measurement [11] and the similar reduction of M(300 K)/M(0 K) is considered in the above-mentioned DMFT and DLM calculations, a larger reduction of spin polarization (SP) at E_F at 300 K relative to SP at 0 K compared to the $M(T)$ behavior indicates that CMS is no longer half-metal at a finite T and that SP at E_F as a function of T is not proportional to $M(T)$. In contrast to the LSDA-DMFT calculations [8], Miyamoto *et al*. [12] have reported no distinct T dependence on the valence band (VB) spectral shape of polycrystalline bulk CMS measured by bulk-sensitive hard x-ray photoemission spectroscopy (HAXPES). Note that the VB spectra in HAXPES generally reflect the Brillouin zone (BZ) averaged density of states (DOS) multiplied by photoionization cross-sections

[13]. In our previous work [14], bulk-sensitive spin-resolved VB HAXPES measurements have revealed that *SP* at E_F of ~90% at T = 21 K is almost independent on T for an epitaxial CMS(001) film up to 300 K, in sharp contrast to the strong T-dependence of *SP* at E_F reported in the LSDA-DLM calculations [9]. Thus, further investigation on the electronic structures and magnetic properties are required to understand the strong T-dependent TMR ratio. One suspects that the electronic and magnetic states near the insulator/half-metal interfaces play an important role in the strong T-dependent TMR ratio, as already reported in several theoretical studies on the CMS/MgO/CMS and related structures at T = 0 K [15-19].

Very recently, the experimental depth-dependent HAXPES measurements combined with x-ray total reflection (TR) for an AlO_x-capped epitaxial CMS(001) thin film at RT have reported the slight changes in the VB spectral shapes of CMS between the near-interface region of the AlO_x/CMS heterojunction and the inside of the CMS film (bulk region) [20]. In addition to the changes in the spectral shapes, the results for the Co and Mn 2*p* core-level magnetic circular dichroism (MCD) in HAXPES have revealed that both the Co and Mn magnetic moments along the easy M axis of the CMS in near-interface region reduces to ~0.77 times compared to those in the bulk region. The possible origin of the changes in the VB spectral shapes and M between the near-interface and bulk regions is considered to be enhanced spin-wave excitations near the interface due to the weakened exchange interaction between the local magnetic moments near the interface compared to the bulk region. To clarify the impact of spin-wave excitations, observations of the T-dependent electronic and magnetic states of CMS in the near-interface and bulk regions by HAXPES are a fairly straightforward way.

In this work, we focus on the T-dependent electronic states of the near-interface of CMS adjacent to the AlO_x layer (near-interface region) and the inside of the CMS film (bulk region) of the AlO_x capped CMS(001) film, which were obtained by using TR- and non-TR-HAXPES, respectively, in a

non-destructive way. In addition, MCD-HAXPES was used as an element specific probe for *M* like MCD in x-ray absorption spectroscopy (XAS). XAS-MCD is a useful technique to determine the spin and orbital magnetic moments through the magneto-optical sum rule with an appropriate assumption of the number of holes in outer shells [21, 22]. On the other hand, MCD-HAXPES gives a relative *M*, which is proportional to the magnitude of MCD signal, and it is possible to detect the relative changes of *M* against a depth from the interface in combination of TR. Information about *M* of the near-interface and bulk regions of the AlO_x/CMS structure was obtained by the Co and Mn 2*p* core-level MCD-HAXPES measurements at $T = 20$ K and was compared with the MCD-HAXPES results at $T = 300$ K [20]. The magnetization of CMS in the bulk region was almost *T*-independent, while that in the near-interface region showed faster demagnetization with increasing *T*. The VB HAXPES spectra of the CMS film clearly showed the changes in the VB spectral shapes in both the bulk and near-interface regions, while the spectra for the near-interface region differ from those for the bulk region. The *T*-dependent VB spectral shapes and *M* behaviors suggested the importance of the spin-wave excitations on the electronic and magnetic states of CMS at a finite *T*, and the enhancement of the spin-wave excitations near the interface compared to the bulk region was confirmed.

II. Experiment

Two CMS epitaxial film samples were prepared by using an ultrahigh vacuum (UHV) sputtering system. One sample is a 30-nm-thick $L2_1$-ordered CMS(001) film grown on a MgO(001) substrate, in which the CMS top layer is covered with an AlO_x(3 nm) layer for the HAXPES measurements. The other sample is a 30-nm-thick $L2_1$-ordered CMS(001) film grown on a Ag(001)/Cr(001)/MgO(001) substrate, where a Ag (Cr) layer thickness is 80 (30) nm, and the CMS surface is covered with a AlO_x(1 nm) layer, for the soft x-ray angle-resolved photoelectron

spectroscopy (SX-ARPES) measurements. The AlO_x films act as a protection layer and form an insulator/ferromagnet heterointerface. The saturation magnetic moment, remanent to saturation M ratio (M_r/M_s), coercivity of the CMS films along the [100] direction (easy M axis) of the CMS film on the MgO(001) substrate are ~4.3 μ_B, ~0.97, and ~16.5 Oe, respectively, and those on the Ag/Cr/MgO(001) are ~4.0 μ_B, ~0.99, and ~10.0 Oe, respectively. Details of sample preparation and characterization have been reported in our previous work [14,20].

The MCD-HAXPES measurements of the AlO_x(3 nm)/CMS(30 nm)/MgO(001) sample for the Co and Mn 2*p* core-level regions were performed at the revolver undulator beamline BL15XU [23,24] of SPring-8. The used sample was identical to that used in the previous MCD-HAXPES measurements [20]. The sample T was kept at 20 K during the MCD-HAXPES measurements. The sample was magnetized *in situ* applied a magnetic field of 3 kOe along the [100] direction of the CMS film in an analysis chamber for HAXPES. The left-and right-handed circularly polarized (LCP and RCP) x-rays with the photon energy ($h\nu$) of 5.95 keV were used to observe MCD in the core-level HAXPES measurements for the sample in a M_r state, where the degree of circular polarization (P_C) was ~0.95 for both LCP and RCP x-rays [25].

The T-dependent VB HAXPES measurements for the AlO_x(3 nm)/CMS(30 nm)/MgO(001) sample, which was prepared by the same procedure as mentioned in Ref. [20], were performed at the undulator beamline BL09XU [26] of SPring-8. The horizontal and vertical linear polarized (H-pol and V-pol) x-rays were used to observe the polarization-dependent VB HAXPES spectra at T = 20, 100, 200, and 300 K with $h\nu$ of 5.95 keV. The degree of linear polarization (P_L) for H-pol and V-pol x-rays were ~1.00 and ~0.90, respectively [26].

The x-ray band width of 5.95 keV x-rays was reduced to below 100 meV by Si(111) double crystal monochromator and post Si 333 channel-cut monochromator (CCM) at BL15XU or post Si 311 double CCM at BL09XU. The H-pol x-rays produced from planar undulators were converted to

obtain the LCP, RCP, and V-pol x-rays by using a diamond phase retarder at both the beamlines. A nearly normal emission geometry was adapted in all HAXPES measurements, where the [100] direction of CMS films was nearly parallel to the incident x-rays and the ***E***-vector of H-pol x-rays was nearly parallel to the surface normal (the [001] direction) of the CMS film. The photoelectrons were detected and analyzed by a high-resolution hemispherical electron analyzer (VG Scienta R4000) in an angle-integrated transmission mode with the acceptance angle of approximately ±7°. The experimental configuration of HAXPES in this work is shown in Fig. S1 in Supplemental Material [27]. Total energy resolution (ΔE) of HAXPES was set to ~150 meV, which was verified by the Fermi edge of an evaporated Au film.

The electronic and magnetic states of the near-interface region of AlO_x/CMS and the bulk region of the buried CMS film were obtained by the HAXPES measurements in the TR and non-TR conditions, respectively. The incidence angles (θ) with respect to the sample surface were set to 0.368° and 2.0° for TR and non-TR conditions, respectively. The θ was referred to the calculated TR critical angle (θ_C) of CMS (0.505°) according to Ref. [34], where experimental θ_C was found by the intensity maximum of the Co 3*s* photoemission as a function of the sample rotation angle as described elsewhere [35]. To numerically estimate the effective inelastic mean-free-path (IMFP) of photoelectrons (λ_{eff}) in the TR and non-TR conditions, IMFP of electrons (λ_e) and x-ray attenuation length (λ_p) were calculated according to Refs. [34-36], resulting $\lambda_{eff} = \lambda_e \cdot \lambda_p / (\lambda_e + \lambda_p)$. Since λ_e and λ_p depend on the kinetic energy of photoelectrons and θ, respectively, λ_{eff} also depends on these parameters.

The AlO_x(1 nm)/CMS(30 nm)/Ag(80 nm)/Cr(30 nm)/MgO(001) sample was used for SX-ARPES, since the thin AlO_x capping layer was suitable due to shorter λ_e (~1 nm) in solids for the SX excitation. The measurements were performed at the twin-helical undulator beamline BL25SU [37] of SPring-8. The ΔE and angular resolution in SX-ARPES by using a high-resolution electron analyzer (VG

Scienta DA30) were set to ~80 meV and ~0.2°, respectively. To probe the Γ-X direction in the momentum space of CMS at T = 30 K, $h\nu$ of 455 and 552 eV was selected according to our previous work [20]. Both the LCP and RCP x-rays were used simultaneously to prevent from detecting magnetic and/or non-magnetic circular dichroism in SX-ARPES for the band dispersion of CMS underneath the AlO_x layer. The reported P_C was ~0.96 [38]. The θ was set to 5° to avoid TR in SX region. For both HAXPES and SX-ARPES, the binding energy (E_B) was referred to E_F of Au.

III. Theoretical calculations

The T-dependent partial DOSs (PDOSs) of the d(xy, yz, zx, x^2-y^2, $3z^2$-r^2), p(x, y, z), and s orbitals for each element in $L2_1$-ordered CMS were used to the VB HAXPES simulations with considering the matrix element (ME) effect [39], where the PDOSs were the same data in Ref. [9]. Since the epitaxial CMS film is used in this work, the ME effect, which gives the photoelectron angular distribution for each atomic orbital, cannot be negligible for the polarized x-ray excitation in the simulation of VB HAXPES spectra. As described in Ref. [9], the multiple-scattering Green's function formalism in the Korringa-Kohn-Rostoker method [40,41], which was implemented by HUTSEPOT code [42], was used to calculate the spin-polarized electronic states of CMS at zero temperature. The spin-polarized electronic states at a finite T, in which the spin fluctuations within the mean-field approximation were treated, were obtained by the DLM method [43] with LSDA [44]. Details of the LSDA-DLM calculations for CMS were given in Ref. [9].

To treat the x-ray polarization dependence in the simulation for the VB HAXPES spectra of CMS, the photoelectron angular distributions (*i.e.* ME effect) for *s*, p(*x, y, z*), and d(*xy, yz, zx,* x^2-y^2, $3z^2$-r^2) orbitals in the dipole approximation with including photoelectron diffraction (PED) effect [45] for H-, V-, and C-pol x-rays were calculated. The energy of photoelectron and the radius of spherical CMS cluster were set to 5945 eV and ~1.7 nm, respectively. The photoelectron intensity in the

acceptance angle (~0.06 sr) of the electron analyzer for HAXPES with respect to that in 4π sr was used to evaluate the photoionization cross-section with including the ME effect. Here, the cross-section of each atomic orbital at $h\nu$ = 6 keV for 4π sr was obtained from Ref. [46]. The sum of the PDOSs multiplied by the cross-sections for each atomic orbital with including ME (*i.e.* ME weighted DOS: MEW-DOS) enables us to compare the theoretical and experimental electronic states of CMS. The MEW-DOSs are convoluted by a Lorentzian function [full width at half maximum (FWHM) varying ~$0.24\times E_B$ (eV)] [14,25], then are multiplied by the Fermi-Dirac function at a finite T, and finally are convoluted by a Gaussian function (FWHM of ΔE in the HAXPES experiments) to simulate the polarization- and T-dependent VB HAXPES spectra of CMS.

IV. Results

A. Core-level MCD-HAXPES spectra of AlO_x/CMS(001) film

Figure 1 shows the Co and Mn 2*p* core-level HAXPES spectra for the AlO_x(3 nm)/CMS(30 nm)/MgO(001) structure measured with LCP and RCP x-rays in the non-TR and TR conditions at T = 20 K. The intensity difference between the LCP and RCP spectra is defined as MCD. In Figs. 1(a) and 1(b), the Co 2*p* HAXPES and MCD spectra in the non-TR and TR conditions are similar each other and are similar to those measured at T = 300 K [20]. These similarities are also seen in the Mn 2*p* HAXPES and MCD spectra in Figs. 1(c) and 1(d). The spectral shapes of the Co (Mn) 2*p* MCD depend on neither TR, non-TR, nor T except the magnitude of MCD. The MCD in the $2p_{3/2}$ region shows the negative-to-positive sign change with increasing E_B and shows opposite behavior in the $2p_{1/2}$ region in both Co and Mn regardless of λ_{eff}. The same sign changes in the Co and Mn 2*p* MCD spectra at T = 20 K in the non-TR and TR conditions indicate that the Co and Mn M's are parallel each other. In Figs. 1(a) and 1(b), the Co 2*p* HAXPES spectra show the satellite (hump) structure in the higher E_B side of both the $2p_{3/2}$ and $2p_{1/2}$ main peaks as indicated by the red

arrows. This hump structure has been commonly observed in Co-based Heusler alloys [47-50], but the origin of the hump structure is unclarified yet. In Fig. 1(e), this hump shows positive (negative) MCD in the $2p_{3/2}$ ($2p_{1/2}$) region indicated by the red arrows. In contrast, the Fe 2*p* HAXPES spectra show the tail structure in the higher E_B side of both the $2p_{3/2}$ and $2p_{1/2}$ main peaks as indicated by the blue arrows as shown in Figs. 1(c) and 1(d). This tail structure shows also positive (negative) MCD in the $2p_{3/2}$ ($2p_{1/2}$) region indicated by the blue arrows in Fig. 1(f). A possible origin of the hump structure in the Co 2*p* HAXPES spectra in CMS is due to the multiplet structures, which depend on the number of 3*d* electrons, in the photoemission final states; the multiplet states in the final states cannot be ignored for a metal with relatively localized 3*d* orbital. Detail discussion is described in Ref. [27].

Since core-level MCD in HAXPES is an element specific method and is proportional to *M* projected onto the incident x-ray direction (see Fig. S1 in Ref. [27]), the element-, *T*-, and λ_{eff}-dependent *M*'s of CMS are evaluated and illustrated in Fig. 2. Here, the magnitude of huge negative Mn (Co) $2p_{3/2}$ MCD is normalized by the Mn (Co) $2p_{3/2}$ main peak height in the sum of the LCP and RCP HAXPES spectra, and *M* (*i.e.*, magnitude of MCD) of each element is normalized at $T = 20$ K in the non-TR condition (bulk region). The magnitude of MCD at $T = 300$ K was taken from Ref. [20]. The magnitudes of MCD in the non-TR condition (λ_{eff} ~6 nm) for both Co and Mn agree with the normalized *M* curve as a function of *T* [$m(T) = 1-\alpha T^{3/2}$ with $\alpha = 2.81\times10^{-6}$ $K^{-3/2}$] for the bulk CMS single crystal reported in Ref. [11], while those in the TR condition (λ_{eff} ~2 nm) are smaller compared to the results in the non-TR condition. For the TR condition (near-interface region), the magnitude of MCD follows $m(T) = 0.825(1-\alpha T^{3/2})$ with $\alpha = 1.46\times10^{-5}$ $K^{-3/2}$. The value of α in the near-interface region is ~5 times larger than that in the bulk region. This result indicates that $m(T)$ in the near-interface region ($m(T)_{interf}$) for both Co and Mn faster decreases with increasing *T* compared to $m(T)$ in the bulk region ($m(T)_{bulk}$) due to larger spin-wave excitations in the near-interface

region. Note that $m(T)_{interf}$ does not approaches to that for the CMS film inside even at $T = 0$ K; $m(0\ \mathrm{K})_{interf}$ is 0.825 times of $m(0\ \mathrm{K})_{bulk}$.

B. Polarization-, *T*- and λ_{eff}-dependent VB HAXPES spectra of AlO_x/CMS(001) film

Figure 3(a) shows the VB spectra of the AlO_x(3 nm)/CMS(001) film measured at $T = 20 – 300$ K in the non-TR condition with λ_{eff} ~6.9 nm (bulk region) for H-pol x-rays. The spectra commonly showed the shoulder (labeled *A*) near E_F, small peak (*B*) at E_B ~0.7 eV, main peak (*C*) at ~1.3 eV, shoulder (*D*) at ~1.8 eV, and small hump (*E*) at ~2.7 eV. As refereed to the spectrum at $T = 20$ K, the intensity of peak *C* decreased with increasing *T*. The decrease of peak *C* intensity was also confirmed from the intensity difference spectra of $I(T–20\mathrm{K})$ in the figure. The *T* dependence on the VB spectral shapes measured at $T = 20$ and 100 K is very weak. A discontinuous change in the spectral shape occurs at *T* between 100 and 200 K, and again the *T* dependence on the spectral shape is very weak at $T = 200$ and 300 K. Figure 3(b) shows the VB spectra of the CMS film measured at $T = 20 – 300$ K in the non-TR condition (bulk region) for V-pol x-rays to clarify the contribution of atomic orbitals in the VB spectra. The changes in the spectral shapes against *T* exist but are very weak compared to the case of H-pol x-rays.

In the VB spectra for V-pol x-rays (Fig. 3(b)), the shoulder *D* and the hump *E* were weakened, the peaks *B* and *C* were broadened, and the shoulder *A* was reduced in comparison with the VB spectrum for H-pol x-rays (Fig. 3(a)). These changes suggest that the shoulders *A* and *D* and hump *E* involve an *s* orbital like band character and that peaks *B* and *C* appear as different *d* orbital symmetries by the change of x-ray polarization. The calculated polarization-dependent cross-sections including ME and PED effects in Table I show that a major (minor) contribution of the Co and Mn 3*d* orbitals is the $3z^2$-r^2 (*yz* and *zx*) component for H-pol x-rays, while the major (minor) contribution of the *yz* ($3z^2$-r^2) component in the 3*d* orbitals is found in V-pol x-rays. In addition, the Co 4*s*, Mn 4*s*, and Si 3*s* show

huge (small) cross-section for H-pol (V-pol) x-rays, which is a characteristic of HAXPES [25,51-53]. Thus, the polarization-dependent HAXPES measurements help to clarify the atomic orbital symmetries in the VB spectra.

Figures 3(c) and 3(d) show the *T*-dependent VB spectra of the AlO_x(3 nm)/CMS(001) film for the near-interface region measured with H- and V-pol x-rays, respectively, in the TR condition (λ_{eff} ~2.0 nm). For comparison, the VB spectra for bulk region at T = 20 K in Figs. 3(a) and 3(b) were overlaid in Figs. 3(c) and 3(d), respectively. The intensity difference spectra of $I(T–20K)$ and the difference spectrum between the interface and bulk regions at T = 20 K denoted by I(interf–bulk) for H-pol x-rays were also shown in Fig. 3(c). The large intensity difference in the peak *C* between the VB spectra for the near-interface and bulk regions at T = 20 K was found. In the V-pol x-ray spectra, *T*-dependence on the spectral shapes also exists but is very weak. The intensity of the peak *C* measured with H-pol x-rays for the non-TR and TR conditions in Figs. 3(a) and 3(c) is plotted as a function of T ($I_C(T)_{bulk}$ and $I_C(T)_{interf}$, respectively) in Fig. 3(e), where $I_C(T)$ is normalized by $I_C(20\ K)_{bulk}$. For comparison, the corresponding main peak in the spin-integrated total DOS of $L2_1$-ordered CMS obtained from the LSDA-DLM calculations in Ref. [9] is overlaid in Fig. 3(e). The DOS peak, which is normalized at T = 0 K, monotonously decreases as T increases. The tendency in the DOS peak is similar to the $I_C(T)_{bulk}$, suggesting that the impact of spin fluctuations at a finite T is observed in the *T*-dependent VB HAXPES spectra even in the low T region below $0.4T_C$. The lower $I_C(T)_{interf}$ compared to $I_C(T)_{bulk}$ seems to be similar to the relation between $m(T)_{bulk}$ and $m(T)_{interf}$. It seems that the discontinuous change of $I_C(T)$ between 100 and 200 K relates to the precession angle of the local magnetic moments, and the critical precession angle for discontinuous change might be around 5°, which is given by $\mathrm{acos}(m(150\ K)_{bulk})$, but the origin of the discontinuous change is unclear from the limited *T*-dependent VB experiments. The *T*-dependent electronic and magnetic states of CMS in the bulk and near-interface regions will be discussed later.

C. Simulation of polarization-dependent VB HAXPES spectra of $L2_1$-ordered CMS

To clarify the atomic orbital contribution in the VB spectra of the AlO_x/CMS(001) film for H- and V-pol x-rays, we have carried out the simulation of VB HAXPES spectra with x-ray polarization dependence. The spin- and orbital-resolved PDOSs for $L2_1$-ordered CMS obtained from the LSDA-DLM calculations [9] are shown in Fig. S2 [27]. Note that the DLM calculations were done not for the interface but for bulk CMS. For comparison, Fig. 4 shows the MEW-PDOSs of the Co and Mn 3*d* and 4*s* states, which are obtained by the PDOSs multiplied by the cross-sections including the ME and PED effects listed in Table I for H-, V-pol x-rays. It is obvious that the photoemission intensity, which is proportional to MEW-PDOS, is dominated by the $3d(3z^2\text{-}r^2)$ and 4*s* states for Co and Mn in the HAXPES spectra for H-pol x-rays in the energy range between 0 and 4 eV, regardless of *T*. In contrast, the intensity is mainly due to the 3*d*(*yz*) states with small contribution of the $3d(3z^2\text{-}r^2)$ states of Co and Mn in the spectra for V-pol x-rays. Thus, we see that the VB spectra with polarization dependence is sensitive to the atomic orbital character. Note that the MEW-PDOSs of the Co and Mn 4*p* states are ignored for simplicity, since the Co and Mn 4*p* PDOSs are much weaker than the 3*d* PDOSs and the cross-sections for the 4*p* orbitals in the 3*d* transition metals is expected to be quite small [25].

Figure 5 compares the experimental and simulated VB HAXPES spectra for H-, V-, and C-pol X-rays. The experimental spectra for $T = 20$ and 300 K in the bulk region of the CMS film were plotted, while the simulated spectra of $L2_1$-ordered CMS for $T = 0$ and 300 K were shown in the figure, where the Fermi-Dirac function for 20 K was used in the simulated spectra at $T = 0$ K for comparison with the experimental results. In the simulation, the cross-sections listed in Table I for the Co and Mn 4*s* orbitals were multiplied by 1.3 and that for the Si 3*s* orbital was multiplied by 0.8 in order to reproduce the experimental spectra in the entire VB region for H-, V-, and C-pol x-rays as shown in Fig. S3 [27].

Note that the simulations for V-pol x-rays, P_L = 0.90 (95% of V-pol x-rays with 5% of H-pol x-rays) are taken into account. The simulated spectra for H-pol x-rays in Fig. 5(a) also show the characteristic structures of the labeled *A*–*F* in the experimental spectra. The dashed lines in Fig. 5(a) indicate the correspondence of the structures *A*–*F* between the experimental and simulated spectra. The intensity reduction in the peak *C* in the experiment with increasing *T* is reproduced in the simulated spectra. From the MEW-PDOSs for *T* = 0 K in the Figs. 4(a) and 4(c), one sees that the shoulder *A* and peak *B* are mainly derived from the Co 3*d*($3z^2$-r^2) and 4*s* majority spin states and that the peak *C* is mainly derived from the Co and Mn 3*d*($3z^2$-r^2) majority spin states. The shoulder *D* is considered to arise from the Co 3*d*($3z^2$-r^2) majority and minority spin states and the Co 4*s* minority spin states. The hump *E* (*F*) is mainly due to the Mn 4*s* minority spin states (the Mn 4*s* majority and minority spin states). The above-mentioned assignments for the structures *A*–*F* in the spectra at *T* = 20 K are the same as those at *T* = 300 K, and the reduction of the peak *C* due to the Co 3*d*($3z^2$-r^2) majority spin states with increasing *T* can be seen from the comparison between Figs. 4(a) and 4(e).

D. Band dispersion of AlO_x/CMS(001) film obtained by SX-ARPES

Figure 6 shows the results of the band dispersion along the Γ–X direction for the AlO_x(1 nm)/CMS(001) film by using SX-ARPES measurements taken at *T* = 30 K with $h\nu$ = 455 and 552 eV. The calculated λ_e for the kinetic energy around 500 eV is ~1 nm, which is half of λ_{eff} ~2.0 nm in TR-HAXPES. The band dispersion behaviors in Figs. 6(a) and 6(b) are very similar to the previous SX-ARPES results of the same sample taken at *T* = 250 K [20], but the dispersion features become clearer, which might be due to less thermal broadening effects. The minority spin band (a convex band dispersion with the apex at E_B of 0.26 eV at Γ point) is clearly seen in Fig. 6(a). The energy of apex position (valence band maximum (VBM) of the minority spin states) at 0.26 eV is

slightly larger than 0.24 eV reported in SX-ARPES taken at T = 250 K [20] and is smaller than 0.35 eV as the minority spin VBM reported in spin-resolved HAXPES taken at T = 21 K [14]. This result suggests that the lattice relaxation and thermal expansion of CMS near the interface differ from those of CMS in the bulk region, since the minority spin VBM position is sensitive to the lattice parameter of CMS [54]. Although the intensity at around E_F near X point for $h\nu$ = 455 eV in Fig. 6(a) is weak, "X"-shaped band dispersion across E_F for $h\nu$ = 552 eV with higher intensity due to the majority spin band is observed in Fig. 6(b). In contrast, a high intensity at the apex at Γ point of the convex band for $h\nu$ = 455 eV in Fig. 6(a) becomes weaker for $h\nu$ = 552 eV in Fig. 6(b). These results are consistent with the previous SX-ARPES results taken at T = 250 K. Since the observed features of band dispersions of the CMS film are very similar to those of bulk Co_2MnGe single crystal in SX-ARPES with the $h\nu$ dependence [55] as a predicted half-metal [54], we can safely conclude that the CMS film in the near-interface region at T = 30 K sustains three-dimensional bulk band structure and band dispersion for the possible half-metal as well as T = 250 K.

Figures 6(c) and 6(d) show the momentum (k) integrated SX-PES spectra along the Γ–X ($k_{//[110]}$) direction for $h\nu$ = 455 and 552 eV at T = 30 K obtained from Figs. 6(a) and 6(b), respectively. The k-integrated SX-PES spectra at T = 250 K obtained from Ref. [20] are also shown in the figure for comparison. The spectra for $h\nu$ = 455 and 552 eV clearly show the T dependence in the E_B range between 0 and 1.5 eV. According to the photoionization cross-sections in the soft x-ray region [51], the cross-section ratio of 4*s*/3*d* orbitals for both Co and Mn is less than 0.1 and the cross-sections of the Co 3*d* orbital is twice of the Mn 3*d* one. In addition, the cross-sections of the Si 3*s* and 3*p* orbitals are sufficiently smaller than that of the Co 3*d* orbital. Therefore, the SX-PES spectra mainly reflect the Co 3*d* states, in particular for the Co 3$d(3z^2\text{-}r^2)$ and 3$d(yz)$ by considering the ME effect. The weaker intensity in the higher E_B side of the peak *C* in the SX-PES than HAXPES indicates the less contribution of the Co and Mn 4*s* PDOSs in the SX-PES spectra.

V. Discussion

Firstly, we discuss the M behaviors as a function of T in the bulk and near-interface regions of the AlO_x(3 nm)/CMS(30 nm)/MgO(001) structure. Owing to the high Mr/Ms ratio of ~0.97, the magnitudes of Co and Mn MCD in the bulk region are almost constant in the T range between 20 and 300 K and agree with the $m(T)_{bulk}$ for the bulk CMS single crystal as shown in Fig. 2. In contrast, the magnitude of MCD in the near-interface region faster decreases as T increases in both Co and Mn. This result is natural, since the exchange interaction (or exchange stiffness) between the magnetic moments near the interface is expected to be weaker than that in the bulk region. However, the value of α, which determines the demagnetization, in the near-interface region is ~5 times larger than that in the bulk region. According to the theory on surface magnetism [56,57], α for a freestanding magnetic film surface (and might be for an interface without interactions with a magnetic film surface) is twice of bulk region due to the smaller exchange interaction at surface (J_{surf}) [or at interface (J_{interf})] compared to that in the bulk region (J_{bulk}). Note that the local Co magnetic moment does not depend on T and λ_{eff}, which is judged from the unchanged Co 2p MCD profiles at different T and λ_{eff} (see Fig. S4 in Ref. [27]). The local Mn magnetic moment is also unchanged as well [27]. Thus, we suspect that additional demagnetization factors exist in the AlO_x(3 nm)/CMS(30 nm)/MgO(001) structure in addition to the fact that $m(0\ K)_{interf}$ is 0.825 times of $m(0\ K)_{bulk}$.

In our MCD-HAXPES experiments, the MCD signals reflect the Mr states in the near-interface and bulk regions of the CMS film. Although the high Mr/Ms of ~0.97 in the average of the entire CMS film, a smaller Mr/Ms in the near-interface region cannot be refused in the condition of $J_{interf} < J_{bulk}$. In this case, the reversed (180º) magnetic domains and 90º magnetic domains are formed in the near-interface region, and $m(T)_{interf}$ becomes smaller than $m(T)_{bulk}$. The domain formation seems to explain the small M near the interface, since the MCD signal is proportional to the Mr along the

[100] direction. Another possibility of $m(T)_{interf} < m(T)_{bulk}$ is the spin reorientation or non-collinear M in the near-interface region of the CMS film. The out-of-plane non-collinear M (cant of M) toward perpendicular to the film surface is not expected from the fact that no enhancement of the local Co (Mn) magnetic moment near the interface compared to the bulk region is observed, since such out-of-plane non-collinear M is accompanied by the enhancement of local magnetic moments [58]. Therefore, the out-of-plane non-collinear M near the interface is also not expected as well as the spin reorientation toward the [001] direction of CMS. Thus, we can conclude that the local magnetic moments near the interface mainly lie in the (001) plane of the CMS film. For the in-plane spin reorientation, M parallel to the [110] or [1$\bar{1}$0] directions in the 3-unit-cell region ($3a$ ~1.7 nm) beneath the interface gives 0.825 in $m(0\ \mathrm{K})_{interf}$ deduced from the normalized MCD signals. Here, we assume that the exponential decay of photoemission intensity is given by $\exp(-d/\lambda_{eff})$, where d represents the depth from the interface. Then, the normalized MCD for $d < 3a$ is set to 1.00 (M parallel to the [100] direction) and for $0 < d < 3a$ is set to cos 45º (45 º magnetic domain). For the in-plane non-collinear M near the interface, the net M direction near the interface orients to the [100] direction with the disorder of the local magnetic moment directions, which also reduces the magnitude of MCD near the interface. A detailed description of non-collinear M has been reported in Ref. [59].

Let us consider the relationship between the electronic and magnetic states of the AlO_x(3 nm)/CMS(30 nm)/MgO(001) structure in the near-interface and bulk regions. As can be seen in Figs. 3(a) and 3(c), the VB spectra for H-pol x-rays show the T dependence, and the changes in the spectral shapes are large in the peak C. The spectral shapes on the lower E_B side of the peak C and the peak B also change with T as can be seen in the intensity difference spectra in Figs. 3(a) and 3(c). As shown in Fig. 3(e), the similar T dependence between the peak C intensity for the bulk region and the main peak in the spin-integrated normalized DOS indicates that the T-dependent VB spectral shapes for the bulk region is due to the impact of spin fluctuations (or spin-wave excitations) on the

electronic states in CMS even though the demagnetization at T = 300 K is quite small in the bulk region as shown in Fig. 2. In the difference spectra in Figs. 3(a) and 3(c), one sees that a slight increase of intensity around E_F with increasing T in both the bulk and near-interface regions. This tendency is also seen in the minority spin states near E_F in the T-dependent LSDA-DLM calculations (Fig. 3 in Ref. [9]). Thus, the spin fluctuations play an important role in the electronic states of CMS even at T below $0.4T_C$. Note that the LSDA-DLM calculations were done not for the interface but for bulk CMS. For the near-interface region, $m(0\ \mathrm{K})_{\mathrm{interf}}$ is 0.825 times of $m(0\ \mathrm{K})_{\mathrm{bulk}}$. If the 180 º domains are formed in the near-interface region, $m(0\ \mathrm{K})_{\mathrm{interf}}$ reduces according to the reduction of the net M. In this case, the VB spectral shape or peak C intensity is not modified by the presence of 180º domains because of no difference between the spin-integrated electronic states for the 0º and 180º domains. Similarly, it is reasonable that there is no difference between the electronic states for the 0º, 90º, and 45º domains. Non-collinear M near the interface can be a possible mechanism in the reduced $m(T)_{\mathrm{interf}}$ compared to $m(T)_{\mathrm{bulk}}$ and the difference in the VB spectral shapes between near-interface and bulk regions, since the non-collinear spin arrangement can modify the electronic states of CMS [19] caused by changes in the hybridizations between the Co-Co, Co-Mn, and Mn-Mn 3d electrons even at T = 0 K. The changes in the hybridizations also occur in the lattice relaxation of CMS near the interface as well as J_{interf}. The exchange energy (E_{ex}) between the nearest neighbor spins of $\boldsymbol{S}_i$ and $\boldsymbol{S}_j$ is given by $-2J\boldsymbol{S}_i \bullet \boldsymbol{S}_j$, so that E_{ex} is lower in the non-collinear M than the collinear M. The lowering of E_{ex} due to the non-collinear M state and $J_{\mathrm{interf}} < J_{\mathrm{bulk}}$ causes the softening of the spin-wave excitations, leading to the enhancement of the spin-wave excitations and the increase of α near the interface. While the antisite disorder is unlikely to dominate in the present samples, other subtle structural imperfections (e.g., strain gradients and/or short-range disorder) cannot be entirely excluded and may contribute second-order effects.

Finally, we discuss the VB HAXPES spectra of CMS in the bulk region in comparison with the

simulated ones. As can be seen in Fig. 5, the energy positions of the peak *B*, peak *C*, shoulder *D*, and hump *E* are different between the experimental and simulated VB spectra. This kind of deviations has also been reported in the hard X-ray ARPES (HARPES) results for the Heusler alloys of Co_2MnGa, CMS, and Co_2FeSi [60] and in HAXPES results for CMS [12] and CFGG [61], which arise from the approximation methods in the theoretical band calculations and/or stoichiometry of the alloys in the experiments. Therefore, we do not consider the energy deviations between the experimental and simulated spectra for CMS. Except for the energy deviations, the intensity of the peak *B* is underestimated in the simulations in each polarization. By considering the VB spectral shapes obtained by SX-PES shown in Figs. 6(c) and 6(d) and photoionization cross-sections [51], the large peak *B* in the SX-PES spectra is dominated by the Co $3d(3z^2\text{-}r^2)$ states. The relatively large intensity of the peak *B* in HAXPES spectra in Fig. 5 indicates the underestimation of the Co $3d(3z^2\text{-}r^2)$ PDOS in the LSDA-DLM calculations. The narrow bandwidth of the peak *C* in the SX-PES spectra is consistent with the narrow Co $3d(3z^2\text{-}r^2)$ and Mn $3d(3z^2\text{-}r^2)$ PDOSs at around the energy position of the peak *C* in the calculations, while the peak *C* is broad in the HAXPES spectra. These results suggest that the Co 4*s* and Mn 4*s* PDOSs are underestimated in the calculations. The larger Co 4*s* PDOS can enhance the intensity of the peak *B* and shoulder *A* in the simulated spectra for H- and C-pol x-rays. For V-pol x-rays, the intensity of shoulder *A* is weak in both the experimental and simulated spectra due to the lower cross-section of *s* orbitals compared to H-pol x-rays. Here, we could not evaluate the PED effects on the cluster size of CMS, which are included in the calculations of the cross-sections with the ME effect. The cluster size used in the PED calculations is smaller than λ_e of photoelectrons in order to reduce the computing resources, so that the underestimation or overestimation in the cross-sections listed in Table I cannot be denied. On the other hand, the simulated spectra clearly show the reduction of the peak *C* and the increase of the intensity around peak *B* on both lower and higher E_B sides. Therefore, we conclude that the *T*-dependent spectral

changes in the experiments clearly probe the effects of spin fluctuations for bulk CMS. The shift of the peak *C* toward lower E_B side in the simulated spectra might be correlated with the narrowing of the minority spin gap with increasing *T*, which can be seen in Figs. 4(b) and 4(f) and Ref. [9]. The narrowing of the minority spin gap causes the creation of the states around E_F below the minority spin conduction band minimum [9]. In fact, the slight increase of the intensity near E_F in the VB spectra shown in Figs. 3(a) and 3(c) with increasing *T* is visible as mentioned above. This increase is due to the *s*-orbital minority spin states around E_F introduced by the spin-fluctuations according to Ref. [19], and can be detected by HAXPES owing to the higher *s*-orbital sensitivity than *d*-orbital [25], but it is unclear in the simulated VB spectra in Fig. 5(a) probably due to the underestimation of *s*-like PDOSs in the LSDA-DLM calculations. In our previous work [14], we have reported the almost *T*-independent *SP* at E_F for CMS by spin-resolved HAXPES, but ΔE of 0.65 eV in spin-resolved HAXPES is insufficient to probe such states created with increasing *T*. The development of high-resolution spin-resolved HAXPES is required to clarify the *T*-dependent spin-resolved electronic states of CMS. The combination of high-resolution spin-resolved HAXPES with TR can clarify the *T*-dependent spin-resolved states near the interface, which helps us to reveal the relationship between $m(T)_{interf}$ and *SP* near the interface.

VI. Summary

The *T*- and λ_{eff}-dependent VB spectral measurements of the AlO_x-capped CMS(001) thin films were performed to reveal the electronic states of CMS in the near-interface and bulk regions by high-resolution HAXPES with various x-ray polarization. The *T*- and λ_{eff}-dependent magnetic states of the AlO_x/CMS film were probed by the Co and Mn 2*p* core-level MCD-HAXPES measurements. The near-interface and bulk electronic and magnetic states were obtained by TR- and non-TR-HAXPES, respectively. The x-ray polarization-dependent VB HAXPES clarified the atomic orbital

contributions in the VB spectra by utilizing the ME effect. The changes in the VB spectral shapes of CMS with increasing T were clearly found in both the near-interface and bulk regions, but the VB spectral shapes for bulk region differed from those for the near-interface region. The normalized M along the [100] direction of CMS in the bulk region obtained form MCD-HAXPES agreed with $m(T)_{bulk}$ for the bulk CMS single crystal, while that of CMS in the near-interface region was smaller than $m(T)_{bulk}$ even at T = 20 K and the demagnetization in the near-interface region was faster than the bulk region with increasing T. The difference in the VB spectra and $m(T)$ between the near-interface and bulk regions of CMS relates to that the M state in the near-interface region (*e.g.* non-collinear spin arrangement) differs from the collinear spin arrangement with the high Mr/Ms ratio in the bulk region.

The T-dependent VB spectra of CMS in the bulk region qualitatively agreed with the LSDA-DLM calculations, indicating the importance of the spin fluctuations on the electronic states of bulk CMS at a finite T and the enhanced spin fluctuations (or spin-wave excitations) in the near-interface region of CMS. Thus, we can conclude that the impact of spin fluctuations on the electronic states of CMS at a finite T is detected by HAXPES through the T-dependent VB measurements. These results can be obtained from x-ray polarization- and T-dependent HAXPES combined with TR. Above-mentioned results cannot be obtained from low-resolution spin-resolved HAXPES of CMS [14] and high-resolution HAXPES of CMS performed at only RT [20]. We thus conclude that the direct probing of the T-dependent electronic and magnetic states of the insulator/ferromagnet heterojunctions in a non-destructive way is important to reveal the properties of insulator/ferromagnet heterojunctions for the near-interface and bulk regions at a finite T. On the other hand, it is difficult to reveal the relationship between $M(T)$ and SP at E_F from the spin-integrated VB HAXPES measurements. This relationship is particularly important in the near-interface region in the heterojunctions. To clarify the T-dependent spin-resolved electronic states in the near-interface and

bulk regions for the heterojunctions, the development of high-resolution spin-resolved VB HAXPES is required.

Acknowledgements

The HAXPES and SX-ARPES measurements were performed with the approval of NIMS Synchrotron X-ray Station at SPring-8 (Proposal No. 2020A4701) and JASRI/SPring-8 (Proposal Nos. 2021A1147, 2021B1468, 2022A1120, 2022A1124, and 2022B1630, and 2022B1306). S.U. would like to thank T. Muro, T. Ohsawa, K. Yamagami, and K. Kuroda for technical support in SX-ARPES. This work was partially supported by Tokodai Institute for Elemental Strategy (TIES) and Data Creation and Utilization Type Material Research and Development Project from MEXT, Japan [Grant Nos. JPMXP0112101001, JPMXP1122683430, and JPMXP1122715503] and JSPS KAKENHI [Grant Nos. 20K05336 and 17H06152].

*Corresponding author. Email: UEDA.Shigenori@nims.go.jp

† Present address: National Institute for Advanced Industrial Science and Technology, Tsukuba, Ibaraki 305-8568, Japan

References

[1] B. D. Terris, T. Thomson, Nanofabricatedand self-assembled magnetic structures as data storage media, J. Phys. D: Appl. Phys. **38**, R199 (2005).

[2] S. Bhatti, R. Sbiaa, A. Hirohata, H. Hono, S. Fukami, S. N. Piramanayagam, Spintronics based random access memory: a review, Mater. Today **20**, 530 (2017).

[3] Y. Sakuraba, M. Hattori, M. Oogane, Y. Ando, H. Kato, A. Sakuma, T. Miyaszaki, H. Kubota, Giant tunneling magnetoresistance in Co_2MnSi / Al–O /Co_2MnSi magnetic tunnel junctions, Appl. Phys. Lett. **88**, 192508 (2006).

[4] B. Hu, K. Moges, Y. Honda, H.-x. Liu, T. Uemura, M. Yamamoto, J.-i. Inoue, M. Shirai, Temperature dependence of spin-dependent tunneling conductance of magnetic tunnel junctions with half-metallic Co_2MnSi electrodes. Phys. Rev. B **94**, 094428 (2016).

[5] K. Moges, Y. Honda, H. X. Liu, T. Uemura, M. Yamamoto, Y. Miura, M. Shirai, Enhanced half-metallicity of off-stoichiometric Heusler alloy $Co_2(Mn,Fe)Si$ investigated through saturation magnetization and tunneling magnetoresistance, Phys. Rev. B **93**, 134403 (2016).

[6] J. W. Jung, Y. Sakuraba, T. Sasaki, Y. Miura, H. Hono, Enhancement of magnetoresistance by inserting thin NiAl layers at the interfaces in $Co_2FeGa_{0.5}Ge_{0.5}$/Ag/$Co_2FeGa_{0.5}Ge_{0.5}$ current-perpendicular-to-plane pseudo spin valves. Appl. Phys. Lett. **108**, 102408 (2016).

[7] K. Elphick, W. Frost, M. Samiepour, T. Kubota, K. Takanashi, H. Sukegawa, S. Mitani, A. Hirosawa, Heusler alloys for spintronic devices: review on recent development and future perspectives. Sci. Technol. Adv. Mater. **22**, 235 (2021).

[8] L. Chioncel, Y. Sakuraba, E. Arrigoni, M. I. Katsenelson, M. Oogane, Y. Ando, T. Miyazaki, E. Burzo, A. I. Lichtenstein, Nonquasiparticle states in Co_2MnSi evidenced through magnetic tunnel junction spectroscopy measurements. Phys. Rev. Lett. **100**, 086402 (2008).

[9] K. Nawa, I. Kurniawan, K. Masuda, Y. Miura, C. E. Patrick, J. B. Staunton, Temperature-dependent spin polarization of Heusler Co_2MnSi from the disordered local-moment approach: Effects of atomic disorder and nonstoichiometry, Phys. Rev. B **102**, 054424 (2020).

[10] H. Shinya, S. Kou, T. Fukushima, A. Masago, K. Sato, H. Katayama-Yoshida, H. Akai, First-principles calculations of finite temperature electronic structures and transport properties of Heusler alloy Co_2MnSi. Appl. Phys. Lett. **117**, 042402 (2020).

[11] L. Ritchie, G. Xiao, Y. Ji, T. Y. Chen, C. L. Chien, M. Zhang, J. Chen, Z. Liu, G. Wu, and X. X. Zhang, "Magnetic, structural, and transport properties of the Heusler alloys Co_2MnSi and NiMnSb", Phys. Rev. B **68**, 104430 (2003).

[12] K. Miyamoto, A. Kimura, Y. Miura, M. Shirai, M. Ye, Y. Cui, K. Shimada, H. Namatame, M. Taniguchi, Y. Takeda, Y. Saitoh, E. Ikenaga, S. Ueda, K. Kobayashi, T. Kanomata, Absence of temperature dependence of the valence-band spectrum of Co_2MnSi, Phys. Rev. B **79**, 100405(R) (2009).

[13] C. S. Fadley, Hard X-ray photoemission with angular resolution and standing-wave excitation. J. Electron Spectrosc. Rel. Phenom. **190**, 165 (2013).

[14] S. Ueda, Y. Miura, Y. Fujita, and Y. Sakuraba, Direct probing of temperature-independent bulk-halfmetallicity in Co_2MnSi by spin-resolved hard x-ray photoemission. Phys. Rev. B **106**, 075101 (2022).

[15] Y. Miura, H. Uchida, Y. Oba, K. Abe, M. Shirai, Half-metallic interface and coherent tunneling in Co_2YZ/MgO/Co_2YZ (YZ = MnSi, CrAl) magnetic tunnel junctions: A first-principles study, Phys. Rev. B **78**, 064416 (2008).

[16] B. Hülsen, M. Scheffer, P. Kratzer, Structural stability and magnetic and electronic properties of Co_2MnSi(001)/MgO heterostructures: A density functional theory study, Phys. Rev. Lett. **103**, 046802 (2009).

[17] A. Sakuma, Y. Toga, H. Tsuchiura, Theoretical study on the stability of magnetic structures in the surface and interfaces of Heusler alloys, Co_2MnAl and Co_2MnSi, J. Appl. Phys. **105**, 07C910 (2009).

[18] T. Saito, T. Katayama, T. Ishikawa, M. Yamamoto, D. Asakura, T. Koide, Y. Miura, M. Shirai, Interface structure of half-metallic Heusler alloy Co_2MnSi thin films facing an MgO tunnel barrier determined by x-ray magnetic circular dichroism, Phys. Rev. B **81**, 144417 (2010).

[19]. Y. Miura, K. Abe, M. Shirai, Effects of interfacial noncollinear magnetic structures on spin-dependent conductance in Co_2MnSi/MgO/Co_2MnSi magnetic tunnel junctions: A first-principles study, Phys. Rev. B **83**, 214411 (2011).

[20] S. Ueda, Y. Fujita, and Y. Sakuraba, Near-interface electronic and magnetic states of insulator/Co_2MnSi heterostructures probed by hard x-ray photoemission combined with x-ray total reflection, Phys. Rev. B **109**, 085109 (2024).

[21] B. T. Thole, P. Carra, F. Sette, G. van der Laan, X-ray circular dichroism as a probe of orbital magnetization, Phys. Rev. Lett. **68**, 1943 (1992).

[22] P. Carra, B. T. Thole, M. Altarelli, X. Wang, X-ray circular dichroism and local magnetic fields, Phys. Rev. Lett. **70**, 694 (1993).

[23] S. Ueda, Application of hard X-ray photoelectron spectroscopy to electronic structure measurements for various functional materials. J. Electron Spectrosc. Rel. Phenom. **190**, 235 (2013).

[24] S. Ueda, K. Katsuya, M. Tanaka, H. Yoshikawa, Y. Yamashita, S. Ishimaru, Y. Matsushita, and K. Kobayashi, Present status of the NIMS contract beamline BL15XU at SPring-8, AIP Conf. Proc. **1234**, 403 (2010).

[25] S. Ueda and I. Hamada, Polarization dependent bulk-sensitive valence band photoemission spectroscopy and density functional theory calculations: Part I. 3*d* transition metals, J. Phys. Soc. Jpn. **86**, 124706 (2017).

[26] A. Yasui, Y. Takagi, T. Osaka, Y. Senba, H. Yamazaki, T. Koyama, H. Yumoto, H. Ohashi, K. Motomura, K. Nakajima, M. Sugahara, N. Kawamura, K. Tamasaku, Y. Tamenori, and M. Yabashi, BL09XU: an advanced hard X-ray photoelectron spectroscopy beamline of SPring-8, J. Synchrotron Rad. **30**, 1013 (2023).

[27] See Supplemental Material at link given by publisher for the experimental geometry of HAXPES, calculated spin- and orbital-resolved PDOSs of $L2_1$-ordered CMS at T = 0 and 300 K, the experimental HAXPES spectra in the entire VB region for H-, V-, and C-pol x-rays at T = 20 and 300 K, and simulated HAXPES at T = 0 and 300 K. Discussion on the satellite structure in the Co 2*p* HAXPES spectra of CMS is also described. It also includes Refs. [9, 20, 25, 28-32, 47-50]. Here, Refs. [28-32] listed below appear only in the Supplemental Materials.

[28] S. Hüfner, *Photoelectron Spectroscopy* (Springer-Verlag, Berlin 2003), 3rd ed.

[29] J. G. Menchero, Spin Polarization and Magnetic Circular Dichroism in Photoemission from the 2*p* Core Level of Ferromagnetic Ni, Phys. Rev. Lett. **76**, 3208 (1996).

[30] Y. Saitoh, S. Ueda, T. Muro, S. Imada, S. Suga, A. Kimura, A. Kakizaki, Magnetic linear dichroism in angle-resolved photoemission of nickel, Phycica B **237-238**, 397 (1997).

[31] G. van der Laan, S. S. Dhesi, E. Dudzik, On-site Coulomb interaction and exchange solitting in Ni 2*p* photoemission of ferromagnetic nickel. Phys. Rev. B **61**, 12277 (2000).

[32] C. De Nadai, G. van der Laan, S. S. Dhesi, N. B. Brookes, Spin-polarized magnetic circular dichroism in Ni 2*p* core-level photoemission, Phys. Rev. B **68**, 212401 (2003).

[33] S. Ueda, M. Mizuguchi, M. Tsujikawa, M. Shirai, Electronic structures of MgO/Fe interfaces with perpendicular magnetization revealed by hard X-ray photoemission with an applied magnetic field. Sci. Technol. Adv. Mater. **20**, 796 (2019).

[34] B. L. Henke, E. M. Gullikson, and J. C. Davis, X-ray interactions: Photoabsorption, scattering, transmission, and reflection at $E = 50–30{,}000$ eV, $Z = 1–92$. At. Data Nucl. Data Tables **54**, 181 (1993).

[35] S. Ueda, Depth-resolved electronic structure measurements by hard X-ray photoemission combined with X-ray total reflection: Direct probing of surface band bending of polar GaN. Appl. Phys. Express **11**, 105701 (2018).

[36] S. Tanuma, C. J. Powell, and D. R. Penn, Calculations of electron inelastic mean free paths. V. Data for 14 organic compounds over the 50–2000 eV range. Surf. Interf. Anal. **21**, 165 (1994).

[37] T. Muro, Y. Senba, H. Ohashi, T. Ohkochi, T. Matsushita, T. Kinoshita, S. Shin, Soft X-ray ARPES for three-dimensional crystals in the micrometre region, J. Synchrotron Rad. **28**, 1631 (2021).

[38] T. Hirono, H. Kimura, T. Muro, Y. Saitoh, T. Ishikawa, Full polarization measurement of SR emitted from twin helical undulators with use of Sc/Cr multilayers at near 400 eV, J. Electron Spectrosc. Rel. Phenom. **144-147**, 1097 (2005).

[39] S. M. Goldberg, C. S. Fadley, S. Kono, Photoionization cross-sections for atomic orbitals with random and fixed spatial orientation. J. Electron Spectrosc. Rel. Phenom. **21**, 285 (1981).

[40] J. Korringa, On the calculation of the energy of a Bloch wave in a metal, Physica **13**, 392–400 (1947).

[41] W. Kohn, N. Rostoker, Solution of the Schrödinger Equation in Periodic Lattices with an Application to Metallic Lithium, Phys. Rev. **94**, 1111–1120 (1954).

[42] M. Däne, M. Lüders, A. Ernst, D. Ködderitzsch, W.M. Temmerman, Z. Szotek, W. Hergert, Self-interaction correction in multiple scattering theory: application to transition metal oxides, J. Phys. Condens. Matter. **21**, 045604 (2009).

[43] B. L. Gyorffy, A. J. Pindor, J. Staunton, G.M. Stocks, H. Winter, A first-principles theory of ferromagnetic phase transitions in metals, J. Phys. F Met. Phys. **15**, 1337–1386 (1985).

[44] J. P. Perdew, Y. Wang, Accnrate and simple analytic representation of the electron-gas correlation energy, Phys. Rev. B **45**, 13244 (1992).

[45] T. Matsushita, F. Matsui, H. Daimon, and K. Hayashi, Photoelectron holography with improved image reconstruction, J. Electron Spectrosc. Relat. Phenom. **178-179**, 195 (2010).

[46] J. H. Scofield, "Theoretical photoionization cross sections from 1 to 1500 keV" (Tech. Rep. UCRL-51326, Lawrence Livermore Laboratory, 1973).

[47] S. Ouardi, G. H. Fecher, B. Balke, A. Beleanu, X. Kozina, G. Stryganyuk, C. Felser, W. Klöß, H. Schrader, F. Bernardi, J. Morais, E. Ikenaga, Y. Yamashita, S. Ueda, K. Kobayashi, Electronic and crystallographic structure, hard x-ray photoemission, and mechanical and transport properties of the half-metallic Heusler compound Co_2MnGe. Phys. Rev. B **84**, 155122 (2011).

[48] X. Kozina, G. H. Fecher, G. Stryganyuk, S. Ouardi, B. Balke, C. Felser, G. Schönhense, E. Ikenaga, T. Sugiyama, N. Kawamura, M. Suzuki, T. Taira, T. Uemura, M. Yamamoto, H. Sukegawa, W. Wang, K. Inomata, K. Kobayashi, Magnetic dichroism in angle-resolved hard x-ray photoemission from buried layer, Phys. Rev. B **84**, 054449 (2011).

[49] R. Fetzer, S. Ouardi, Y. Honda, H.-x. Liu, S. Chadov, B. Balke, S. Ueda, M. Suzuki, T. Uemura, M. Yamamoto, M. Aeschlimann, M. Cinchetti, G. H. Fecher, C. Felser, Spin-resolved low-energy and hard x-ray photoelectron spectroscopy of off-stoichiometric Co_2MnSi Heusler thin films exhibiting a record TMR. J. Phys. D: Appl. Phys. 48, 164002 (2015).

[50] S. Ouardi, G. H. Fecher, T. Kubota, S. Mizukami, E. Ikenaga, T. Nakamura, C. Felser, Magnetic dichroism study of Mn1.8Co1.2Ga thin film using a combination of x-ray absorption and photoemission spectroscopy, J. Phys. D: Appl. Phys. **45**, 164007 (2015).

[51] J. J. Yeh, I. Lindau, Atomic subshell photoionization cross sections and asymmetry parameters: $1 \leq Z \leq 103$, At. Data Nucl. Data Tables **32**, 1 (1985).

[52] S. Ueda and I. Hamada, Polarization dependent bulk-sensitive valence band photoemission spectroscopy and density functional theory calculations: Part II. 4*d* transition metals, J. Phys. Soc. Jpn. **90**, 034706 (2019).

[53] S. Ueda and I. Hamada, Polarization-dependent bulk-sensitive valence band photoemission spectroscopy and density functional theory calculations: Part III. 5*d* transition metals, J. Phys. Soc. Jpn. **91**, 024801 (2022).

[54] S. Picozzi, A. Continenza, A. J. Freeman, Co_2MnX (X = Si, Ge, Sn) Heusler compounds: An *ab initio* study of their structural, electronic, and magnetic properties at zero and elevated pressure, Phys. Rev. B **66**, 094421 (2002).

[55]. T. Kono, M. Kakoki, T. Yoshikawa, X. Wang, K. Goto, T. Muro, R. Umetsu, A. Kimura, Visualizing half-metallic bulk band structure with multiple Weyl cones of the Heusler ferromagnet, Phys. Rev. Lett. **125**, 216403 (2020).

[56] D. Marui, D. Scholl, H. C. Seigmann, E. Kay, Observation of the exchange interaction at the surface of a ferromagnet, Phys. Rev. Lett. **61**, 758 (1988).

[57] H. C. Siegmann, Surface and 2D magnetism, J. Phys: Condens. Mater. **4**, 8395 (1992).

[58] T. Kawauchi, Y. Miura, X. Zhang, K. Fukutani, Interface-driven noncolliner magnetic structure and phase transition of Fe thin films. Phys. Rev. B **95**, 014432 (2017).

[59] P. J. Jensen, K. H. Bennemann, Magnetic structure of films: Dependence on anisotropy and atomic morphology, Surf. Sci. Rep. **61**, 129 (2006).

[60] S. Chernov, C. Lidig, O. Fedchenko, K. Medjianik, S. Babenkov, D. Vasilyev, M. Jourdan, G. Schönhense, H. J. Elmers, Band structure tuning of Heusler compounds: Spin- and momentum-

resolved electronic structure analysis of compounds with different band filling, Phys. Rev. B **103**, 054407 (2021).

[61] K. Goto, L. S. R. Kumara, Y. Sakuraba, Y. Miura, I. Kurniawan, A. Yasui, H. Tajiri, Y. Fujita, Z. Chen, K. Hono, Effects of the atomic order on the half-metallic electronic structure in the $Co_2Fe(Ga_{0.5}Ge_{0.5})$ Heusler alloy thin film, Phys. Rev. Mater. **4**, 114406 (2020).

Figure captions

FIG. 1. (Color online) Co 2*p* core-level HAXPES and MCD spectra for AlO_x/CMS at $T = 20$ K in the non-TR condition (λ_{eff} ~6.1 nm) (a) and the TR condition (λ_{eff} ~2.0 nm) (b). Mn 2*p* core-level HAXPES and MCD spectra at $T = 20$ K in the non-TR condition (λ_{eff} ~6.3 nm) (c) and the TR condition (λ_{eff} ~2.0 nm) (d). (e) and (f) Enlarged MCD spectra of the Co and Mn 2*p* core-levels in the non-TR condition, respectively. The red (blue) arrows indicate the location of the hump (tail) structures in the Co (Mn) 2*p* HAXPES spectra. The data acquisition time for the Co (Mn) core-level measurement in both the TR and non-TR conditions is ~15 (~20) min, and ΔE is set to ~150 meV.

FIG. 2. (Color online) Comparison between the *T*-dependent normalized magnetization, $m(T)$, and the normalized Co and Mn MCD signals for the bulk (λ_{eff} ~6.9 nm) and near-interface (λ_{eff} ~2.0 nm) regions for the AlO_x/CMS(001) film. The $m(T)$ with $\alpha = 2.81\times 10^{-6}$ shown by black curve is obtained from the bulk CMS single crystal in Ref. [11]. The $m(T)$ with $\alpha = 1.46 \times 10^{-5}$ shown by green curve was obtained from the fitting of the Co and Mn MCD signals at $T = 20$ and 300 K for the near-interface region. The error of α is $\pm 1.5\times 10^{-5}$.

FIG. 3. (Color online) (a) *T*-dependent VB spectra for the bulk region measured with H-pol x-rays in the non-TR condition (λ_{eff} ~6.9 nm). The intensity difference spectra, $I(T–20\text{K})$ with $T = 300$, 200, and 100 K, are also plotted in the figure. (b) Same as (a), but measured with V-pol x-rays. (c) *T*-dependent VB spectra for the near-interface region measured with H-pol x-rays in the TR condition (λ_{eff} ~2.0 nm). The difference spectra of $I(T–20\text{K})$ and $I(\text{interf}–\text{bulk})$ at $T = 20$ K are also plotted in the figure. (d) Same as (c), but measured with V-pol x-rays. The data acquisition time for the VB measurement with H-pol (V-pol) x-rays in both the TR and non-TR conditions is ~20 (~30) min, and ΔE is set to ~150 meV. (e) The normalized peak *C* intensities at E_B ~1.26 eV for $T = 20$, 100, 200, and 300 K in the bulk (λ_{eff} ~6.9 nm) and near-interface (λ_{eff} ~2.0 nm) regions measured with H-pol x-rays in (a) and (c). The statistical errors are indicated by the vertical bars. The corresponding main peak in the spin-integrated total DOSs of $L2_1$-ordered CMS obtained from the LSDA-DLM calculations for $T = 0$, 100, 200, 300, and 400 K [9] is plotted for comparison. The peak DOS is normalized at $T = 0$ K, and the energy window is set to 90 meV.

FIG. 4. (Color online) Co 3*d* and 4*s* MEW-PDOSs of $L2_1$-ordered CMS at T = 0 K (a) and 300 K (e) for H-pol x-rays. (b) and (f) same as (a) and (e), respectively, but for V-pol x-rays. Mn 3*d* and 4*s* MEW-PDOSs of $L2_1$-ordered CMS at T = 0 K (c) and 300 K (g) for H-pol x-rays. (d) and (h) same as (c) and (g), respectively, but for V-pol x-rays. The minority spin MEW-PDOSs are indicated by negative value for visibility.

FIG. 5. (Color online) (a)-(c) Experimental and simulated VB HAXPES spectra of CMS for H-, V-, and C-pol x-rays, respectively. The experimental spectra measured in the non-TR condition (λ_{eff} ~6.9 nm) at T = 20 and 300 K were shown for comparison with the simulated spectra at T = 20 and 300 K. In (b), the experimental P_L is taken into account in the simulation for V-pol x-rays.

FIG. 6. (Color online) SX-ARPES results of the AlO_x(1 nm)-capped CMS(001) thin film measured at T = 30 K for (a) $h\nu$ = 455 eV and (b) 552 eV. The vertical dashed lines indicate the high symmetry Γ or X points. T-dependent k-integrated SX-PES spectra obtained at T = 30 and 250 K along the Γ–X direction for (c) $h\nu$ = 455 eV and (d) 552 eV. The spectra for T = 30 K were obtained from the k-integration of (a) and (b), and those for T = 250 K were obtained in the same way by using the SX-ARPES results in Ref. [20]. The data acquisition time for the ARPES measurement in each $h\nu$ is ~30 min, and ΔE is set to ~80 meV.

Figures

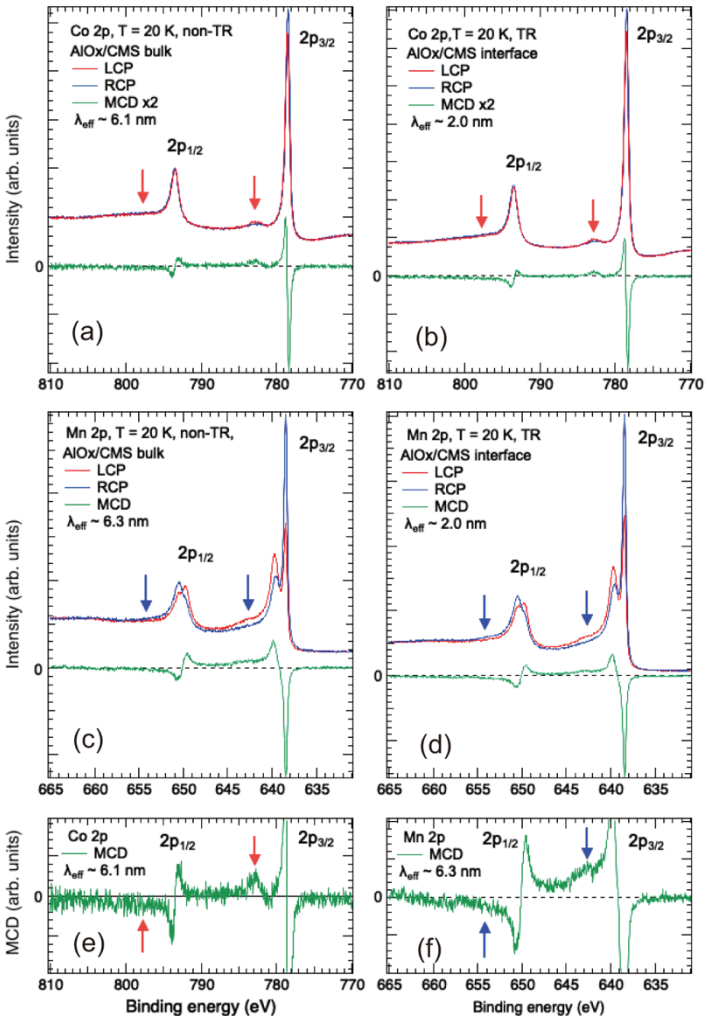

Figure 1

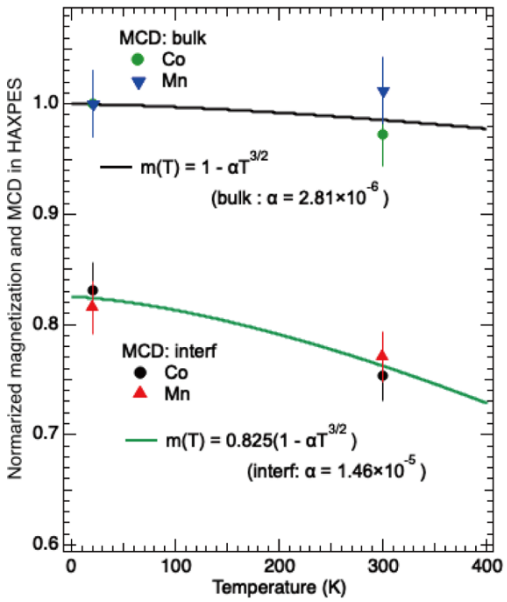
MCD: bulk
Co
Mn
m(T) = 1 - αT^3/2
(bulk : α = 2.81×10^-6)
MCD: interf
Co
Mn
m(T) = 0.825(1 - αT^3/2)
(interf: α = 1.46×10^-5)
Normarized magnetization and MCD in HAXPES
Temperature (K)
1.0
0.9
0.8
0.7
0.6
0
100
200
300
400

Figure 2

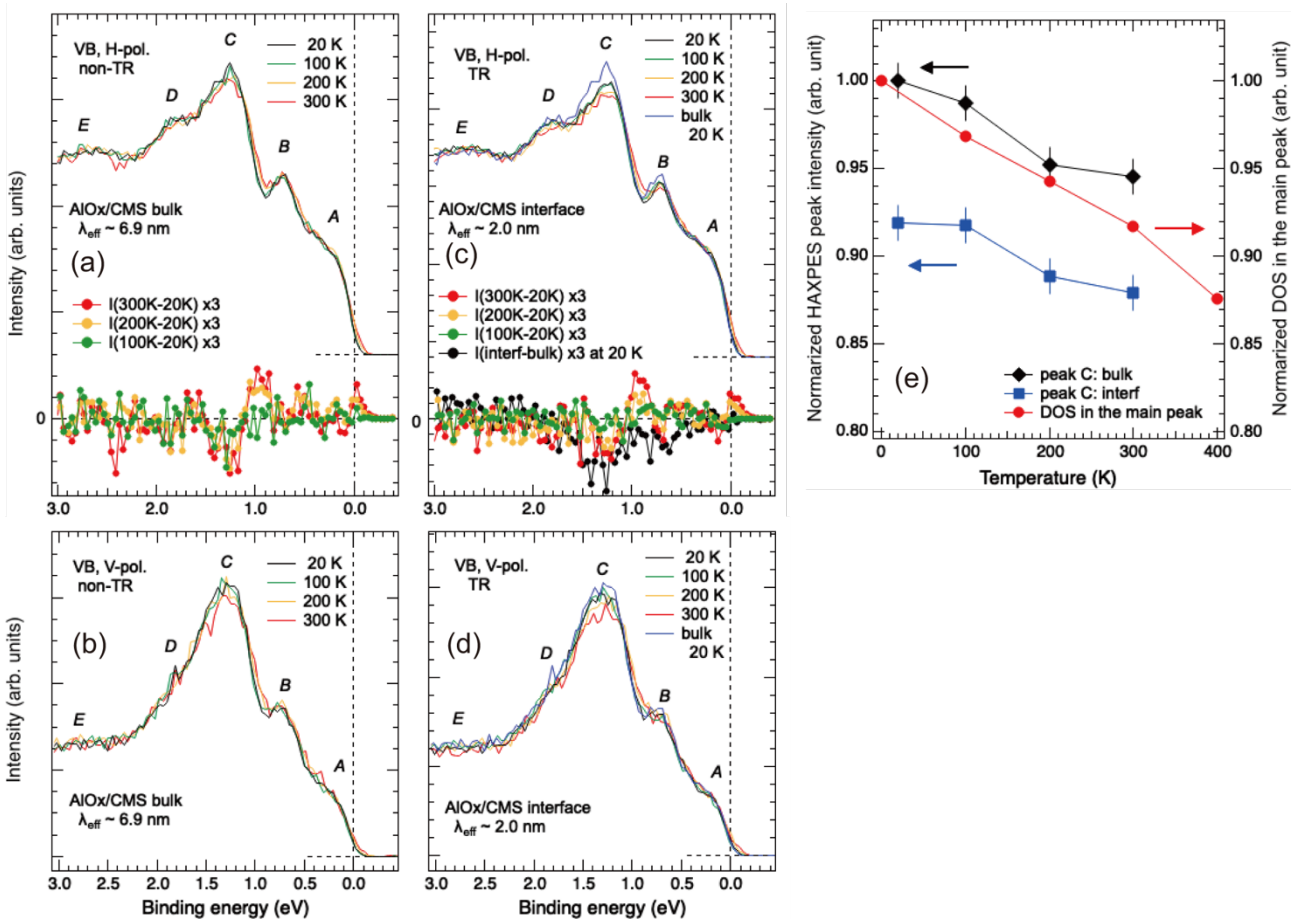
VB, H-pol.
non-TR
20 K
100 K
200 K
300 K
C
D
E
B
A
AlOx/CMS bulk
λeff ~ 6.9 nm
(a)
I(300K-20K) x3
I(200K-20K) x3
I(100K-20K) x3
Intensity (arb. units)
0
3.0
2.0
1.0
0.0
VB, H-pol.
TR
bulk
20 K
AlOx/CMS interface
λeff ~ 2.0 nm
(c)
I(interf-bulk) x3 at 20 K
VB, V-pol.
non-TR
(b)
VB, V-pol.
TR
(d)
3.0
2.5
2.0
1.5
1.0
0.5
0.0
Binding energy (eV)
(e)
peak C: bulk
peak C: interf
DOS in the main peak
Normarized HAXPES peak intensity (arb. unit)
Normarized DOS in the main peak (arb. unit)
1.00
0.95
0.90
0.85
0.80
0
100
200
300
400
Temperature (K)

Figure 3

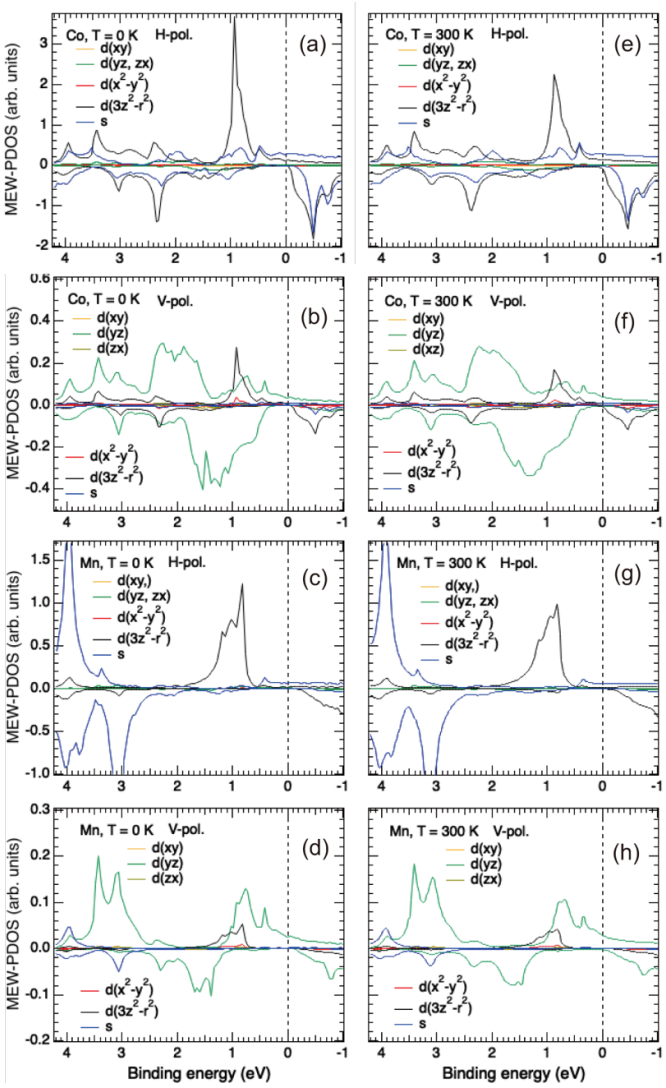
Co, T = 0 K H-pol.
(a)
Co, T = 300 K H-pol.
(e)
Co, T = 0 K V-pol.
(b)
Co, T = 300 K V-pol.
(f)
Mn, T = 0 K H-pol.
(c)
Mn, T = 300 K H-pol.
(g)
Mn, T = 0 K V-pol.
(d)
Mn, T = 300 K V-pol.
(h)
d(xy)
d(yz, zx)
d(x2-y2)
d(3z2-r2)
s
MEW-PDOS (arb. units)
Binding energy (eV)

Figure 4

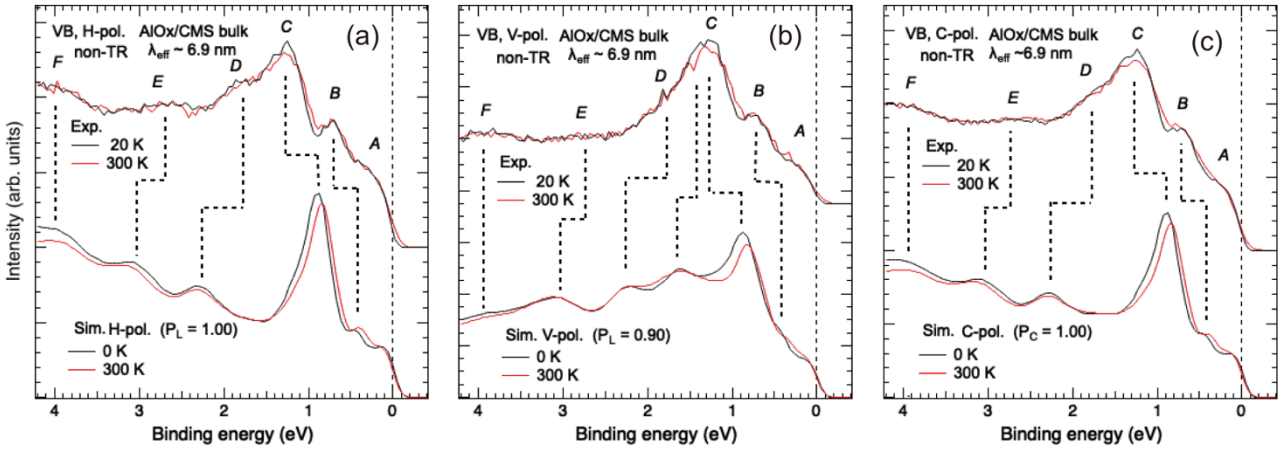
VB, H-pol. AlOx/CMS bulk
non-TR λeff ~ 6.9 nm
(a)
Exp.
20 K
300 K
Sim. H-pol. (PL = 1.00)
0 K
300 K
VB, V-pol. AlOx/CMS bulk
non-TR λeff ~ 6.9 nm
(b)
Exp.
20 K
300 K
Sim. V-pol. (PL = 0.90)
0 K
300 K
VB, C-pol. AlOx/CMS bulk
non-TR λeff ~6.9 nm
(c)
Exp.
20 K
300 K
Sim. C-pol. (PC = 1.00)
0 K
300 K
A
B
C
D
E
F
Intensity (arb. units)
Binding energy (eV)
4
3
2
1
0

Figure 5

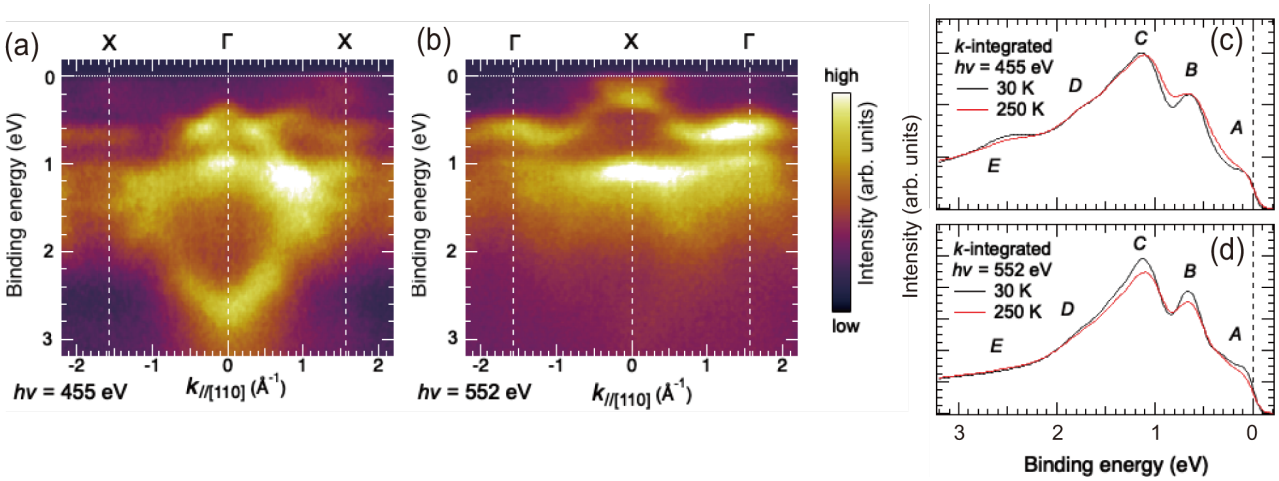
(a)
X
Γ
X
Binding energy (eV)
0
1
2
3
-2
-1
0
1
2
hv = 455 eV
k//[110] (Å-1)
(b)
Γ
X
Γ
hv = 552 eV
high
low
Intensity (arb. units)
(c)
k-integrated
hv = 455 eV
30 K
250 K
A
B
C
D
E
(d)
k-integrated
hv = 552 eV
30 K
250 K
Intensity (arb. units)
3
2
1
0
Binding energy (eV)

Figure 6

Table I: Element- and orbital-dependent relative photoionization cross-sections per electron including ME and PED effects for $L2_1$-ordered CMS for various x-ray polarization. The values are normalized by the Co $3d(3z^2\text{-}r^2)$ cross-section for H-pol x-rays.

			Relative cross-section per electron		
		Polarization	H-pol.	V-pol.	C-pol.
Element	Orbital				
Co	$3d(3z^2\text{-}r^2)$		1.000	7.550e-2	0.5242
	$3d(x^2\text{-}y^2)$		7.438e-3	1.050e-2	9.012e-3
	$3d(xy)$		1.145e-2	1.197e-2	1.172e-2
	$3d(yz)$		0.1068	0.3212	0.2172
	$3d(zx)$		0.1068	1.079e-2	5.738e-2
	$4s$		8.523	0.2157	4.070
Mn	$3d(3z^2\text{-}r^2)$		0.7451	3.245e-2	0.3790
	$3d(x^2\text{-}y^2)$		3.556e-3	5.046e-3	4.327e-3
	$3d(xy)$		6.287e-3	5.095e-2	5.670e-3
	$3d(yz)$		4.573e-2	0.2384	0.1447
	$3d(zx)$		4.573e-2	5.949e-3	2.527e-2
	$4s$		9.894	0.2261	4.703
Si	$3p(x)$		1.047e-2	1.729e-3	5.932e-3
	$3p(y)$		1.047e-2	7.846e-2	4.574e-2
	$3p(z)$		0.3347	9.712e-3	0.1661
	$3s$		11.417	0.2112	5.411